

Circular-hyperbolic skyrmion in rotating pseudo-spin-1/2 Bose-Einstein condensates with spin-orbit coupling

Chao-Fei Liu,^{1,2} Heng Fan,² Yi-Cai Zhang,² Deng-Shan Wang,² and Wu-Ming Liu²

¹*School of Science, Jiangxi University of Science and Technology, Ganzhou 341000, China*

²*Beijing National Laboratory for Condensed Matter Physics, Institute of Physics, Chinese Academy of Sciences, Beijing 100190, China*

(Received 5 September 2012; published 19 November 2012)

By exploring the spin-orbit-coupled rotating pseudo-spin-1/2 Bose-Einstein condensates with the stochastic projected Gross-Pitaevskii equations, we prove the existence of the circular-hyperbolic skyrmion, which possesses two extreme values of S_z . The nonequal intraspecies interactions and interspecies interactions cause the two components to be wholly disproportionate when the system reaches the equilibrium state. The circular-hyperbolic skyrmion results from the vortex-dipole structure. For the miscible condensates, the increase of spin-orbit coupling enhances the creation of the circular-hyperbolic skyrmion, and makes them link one after another locally. In particular, the circular-hyperbolic skyrmion even can form a chain when the spin-orbit coupling is only in one direction. For the immiscible condensates, the hyperbolic skyrmion occurs at the center, while the circular-hyperbolic skyrmion occurs at the outskirts of the condensates. The increase of the spin-orbit coupling restricts the creation of the hyperbolic skyrmion and enhances the creation of the circular-hyperbolic skyrmion.

DOI: [10.1103/PhysRevA.86.053616](https://doi.org/10.1103/PhysRevA.86.053616)

PACS number(s): 03.75.Mn, 05.30.Jp, 03.75.Lm

I. INTRODUCTION

Spin-orbit interaction couples the spin and momentum degrees of freedom, which plays an important role in realizing some new physics such as the spin-Hall effect [1,2], topological insulator [3–5], etc. Recently, spin-orbit coupling (SOC) in Bose gases of ^{87}Rb atom has been observed in experiments [6,7] with the synthetic non-Abelian gauge fields. The SOC effect of the Bose gases provides a new platform for the new physics and the method of manipulating the quantum system, which has attracted much attention [8–15]. For atoms with internal degrees of freedom, their collision interactions generally contain spin dependence, which determines the various ground-state phases. Without SOC, the two-component Bose-Einstein condensates (BECs) can be of either phase separation or phase mixture. The inclusion of SOC induces competition with spin-dependent interactions, in addition to modifying the single-particle spectra of a spinor BEC. As a result, a spin-dependent interaction in turn influences the atomic spatial motion, leading to a variety of density patterns even in the ground state [8–13], such as the stripe phase and the plane-wave phase in the nonrotation BECs.

In this paper, we consider the ultracold bosons with SOC and the rotation under a quenching process. Generally, the combination of SOC and the rotation can cause various vortex lattices [14,15]. For example, Xu *et al.* [14] found that increasing the SOC strength would favor a triangular vortex lattice in the fast rotating BECs. Zhou *et al.* [15] showed that if the trapping potential is strong and the interaction is relatively weak, then a half-quantum vortex lattice is formed under rotation. Many properties of the vortices' structure have been studied, but the properties of the skyrmion, which may concern the vortices in these rotating BECs and is important in our understanding of those systems, have not won enough attention. Furthermore, almost all of the theoretical research, including the above two rotating cases, consider that the intraspecies interactions of both spin-up and spin-down are equal, i.e., $g_1 = g_2$. This implies that the two components

are completely identical. In a real system, the Zeeman shift induces different energies for particles. Competition of the virtually different intraspecies interaction causes the particles to be disproportionate. Thus, the equal intraspecies interaction ($g_1 = g_2$) conflicts with the real competition of particle interactions. So it is of interest to study the more realistic conditions.

The skyrmions are topological solitons, which were originally proposed in the 1960s in nuclear physics by Skyrme to account for baryons as a quasiparticle excitation with spins pointing in all directions to wrap a sphere [16,17]. Skyrmions have been observed in many condensed-matter systems, such as liquid $^3\text{He-A}$ [18], quantum Hall systems [19], liquid crystals [20], and helical ferromagnets [21,22]. Generally, spins of skyrmions are antiparallel to the applied magnetic field at the skyrmion centers and are parallel at their peripheries. For a skyrmion with a topological charge of one, the spin-vector of the skyrmion sweeps the whole unit sphere.

In the two-component BEC, the nonsingular skyrmion is related to the Mermin-Ho coreless vortices [23]. Roughly speaking, the skyrmion is an excitation that can be created out of the ground state, in which all of the spins are aligned, by reversing the average spin in a finite region of space [24,25]. Meanwhile, the arrows of the skyrmions can either form a circular pattern, point to the outside, or point into the center in the two-dimensional plane [26,27]. Typically, the skyrmion is centrosymmetric. It will be interesting to determine if there are some other cases in the two-component BEC with SOC, and to address questions such as: Are there other configurations for a skyrmion? How many different configurations does the skyrmion have? Since a skyrmion is viewed as the reverse of the local spin, are there other types of skyrmions present, such as the noncentrosymmetric configuration?

The purpose of this paper is to summarize the types of skyrmions and discover other skyrmion configurations. By analyzing the solution of the skyrmion and classifying the basic configuration of the skyrmion, we find that some two-extreme-value skyrmions are ignored in the previous

investigation. We estimate the properties of the two-extreme-value skyrmion. Our numerical experiment, which considers the condensate with SOC, proves the scenario and we find the circular-hyperbolic skyrmion, which indeed has two different extreme values. The circular-hyperbolic skyrmions encircle the center of the system and can form some chains locally. These properties indicate the difference between the circular-hyperbolic skyrmion and the normal skyrmion. The distribution of the circular-hyperbolic skyrmion is different from that of the normal skyrmion.

The paper is organized as follows: In Sec. II, we analyze the skyrmion solution and obtain seven different skyrmion configurations. Meanwhile, the analysis implies the presence of the two-extreme-value skyrmion. In Sec. III, we introduce our model, the stochastic projected Gross-Pitaevskii equations, and some initial conditions for our simulations. In Sec. IV, we present our main results and some explanations. In Sec. IV A, we use SOC to induce the vortices and circular-hyperbolic skyrmion in the rotating miscible Bose-Einstein condensates. We illuminate the relationship between the vortex structure and the circular-hyperbolic skyrmion. Meanwhile, we design an experimental scheme, which remains SOC only in the y direction, to obtain the circular-hyperbolic skyrmion chain. In Sec. III B, we show that the circular-hyperbolic skyrmion can occur in the immiscible BECs when the strength of the SOC is strong enough. Meanwhile, along the radius, the hyperbolic skyrmion will transfer to the circular-hyperbolic skyrmion according to the density distribution of the two BECs. A summary of the paper is presented in Sec. V.

II. ANALYSIS OF THE PRESENCE OF TWO-EXTREME-VALUE SKYRMION

We assume there is a skyrmion solution (S_x, S_y, S_z) where $|S|^2 = 1$. For example, we can use Eqs. (1) to represent the skyrmion [27],

$$\begin{aligned} S_x &= \frac{4\lambda x e^{-(x^2+y^2)/2}}{x^2 + y^2 + 4\lambda^2 e^{-(x^2+y^2)/2}}, \\ S_y &= \frac{-4\lambda y e^{-(x^2+y^2)/2}}{x^2 + y^2 + 4\lambda^2 e^{-(x^2+y^2)/2}}, \\ S_z &= \frac{x^2 + y^2 - 4\lambda^2 e^{-(x^2+y^2)/2}}{x^2 + y^2 + 4\lambda^2 e^{-(x^2+y^2)/2}}. \end{aligned} \quad (1)$$

We know that the topological charge Q is a very important value to characterize the spin texture. The topological charge is defined by $Q = \frac{1}{4\pi} \int \mathbf{S} \cdot (\frac{\partial \mathbf{S}}{\partial x} \times \frac{\partial \mathbf{S}}{\partial y}) dx dy$ and the topological charge density is defined as $q(x, y) = \frac{1}{4\pi} \mathbf{S} \cdot (\frac{\partial \mathbf{S}}{\partial x} \times \frac{\partial \mathbf{S}}{\partial y})$. A skyrmion has the topological charge $|Q| = 1$. We have noted that if the solution (S_x, S_y, S_z) can describe a skyrmion, then the solution $(S_x, -S_y, S_z)$ also satisfies the condition to present a skyrmion. The topological charge $|Q|$ of the two skyrmions is equal. Similarly, $(-S_x, S_y, S_z)$, $(S_x, -S_y, -S_z)$, etc. satisfy the condition to construct a corresponding skyrmion with topological charge $|Q| = 1$. Thus, the addition of the minus on the spin vector causes a different skyrmion. In fact, this operation causes eight different skyrmion configurations. Furthermore, if we exchange S_x , S_y , and S_z , then the topological charge $|Q|$ is also conserved [28]. This operation can

cause six configurations. Meanwhile, the topological charge density $|q(x, y)|$ is unchanged under both operations. Thus, combining the two simple operations, we can obtain 48 skyrmion configurations. However, some configurations have similar properties. Thus, we can view them as the same type of skyrmion.

Figures 1(a)–1(g) shows seven types of skyrmions with the above operations by using Eqs. (1). The title of each figure indicates the corresponding spin vector. We can name them radial-out skyrmion, radial-in skyrmion, circular skyrmion, hyperbolic skyrmion, hyperbolic-radial(out) skyrmion, hyperbolic-radial(in) skyrmion, and circular-hyperbolic skyrmion, respectively. We find that other skyrmion configurations can be presented by the seven basic configurations [Figs. 1(a)–1(g)] with the rotation, the image with the y axis, and the exchange of the color. For example, the skyrmion in Fig. 1(h) is the same type as that in Fig. 1(g). When we rotate Fig. 1(g) $-\pi/2$ anticlockwise, and exchange the color of the arrows and image with the y axis, we can obtain Fig. 1(h). We can present Fig. 1(h) as $-g'(-\pi/2)$, where g denotes that Fig. 1(h) is the same type as Fig. 1(g), the $-$ symbol denotes the exchange of the color of the arrows (an imaging with the x - y plane), and g' denotes the imaging with the y axis. Table I shows all of the skyrmion configurations from Fig. 1. The column headings indicate the plus and minus of the three spin vectors, and the first column is the form of the three spin vectors of Eqs. (1).

The skyrmion is the spin defect. The outer arrows in Figs. 1(a)–1(d) are standing up. Meanwhile, the skyrmions in Figs. 1(a)–1(d) have only one extreme value. These figures factually show the normal skyrmion which has appeared in many previous studies [26,27]. However, the ambient arrows in Figs. 1(e)–1(h) are accumbent in the x - y plane. These skyrmions have two extreme values of S_z : a minima and a maximum. Figure 1(e) is a combination of a radial-out structure and a hyperbolic one. Thus we can call it the hyperbolic-radial(out) skyrmion. Similarly, Fig. 1(f) indicates a hyperbolic-radial(in) skyrmion. Figure 1(g) can be viewed as a combination of a circular and a hyperbolic structure. Hence we can call it the circular-hyperbolic skyrmion. Figure 1(h) also plots a circular-hyperbolic skyrmion since it has a similar configuration to Fig. 1(g).

With Eqs. (1), the vectors $(\pm S_x, \pm S_y, \pm S_z)$ and $(\pm S_y, \pm S_x, \pm S_z)$ produce 16 skyrmions, which have only one extreme value. Meanwhile, they can be characterized by Figs. 1(a)–1(d) with the rotation, the image with the y axis, and the exchange of the color. There are 32 two-extreme-value skyrmions, which can be presented by Figs. 1(e)–1(g) with the rotation, the image with the y axis, and the exchange of the color. Furthermore, we summarize all of the possible configurations of the skyrmion in Table I using Figs. 1(a)–1(g). Now, we can conclude that it is possible to realize the two-extreme-value skyrmions. At least we have obtained the configuration to characterize them. The two-extreme-value skyrmion must not result from the vortex-core structure (Mermin-Ho vortex) simply since it is not centrosymmetric. Figures 1(e)–1(g) imply that some special structure induces the two-extreme-value skyrmion. And we can guess that it should be some dipole structure. If it is related to the dipole structure, such as the Anderson vortex (rather than the normal Anderson vortex [33,34]), then it would be

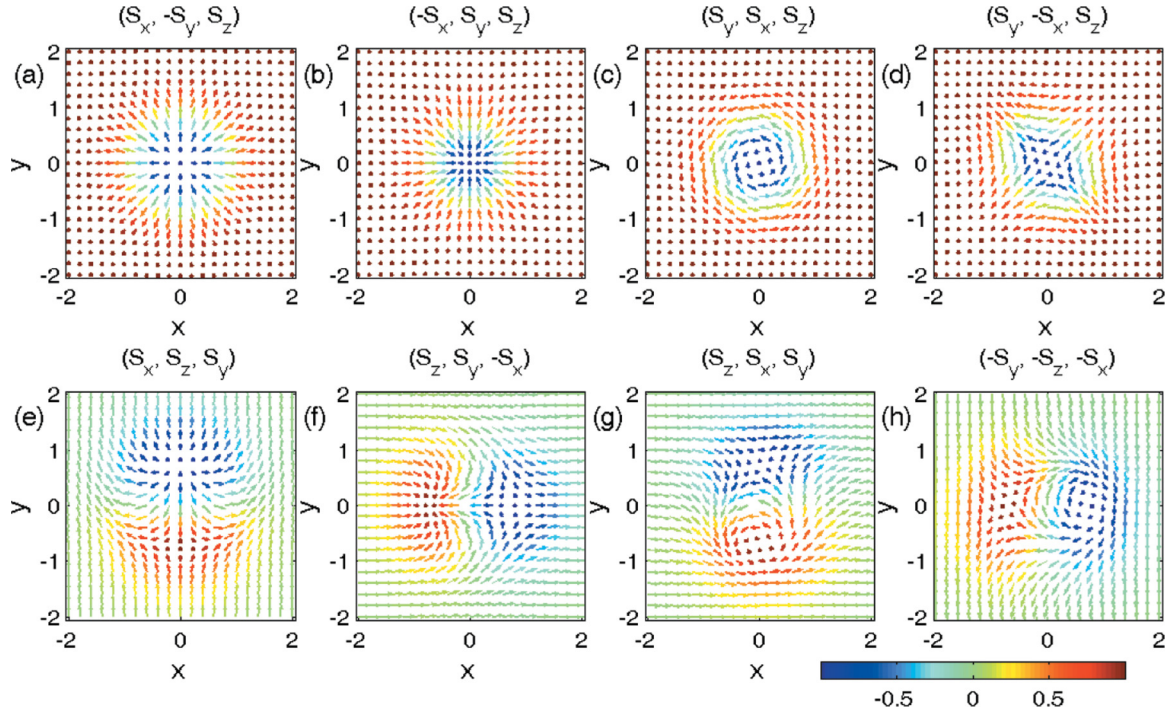


FIG. 1. (Color online) Configuration of the skyrmion with Eqs. (1), where $\lambda = 0.5$. The subfigures indicate the mode of the spin vectors: (a) radial-out skyrmion, (b) radial-in skyrmion, (c) circular skyrmion, (d) hyperbolic skyrmion, (e) hyperbolic-radial(out) skyrmion, (f) hyperbolic-radial(in) skyrmion, (g) circular-hyperbolic skyrmion I, and (h) circular-hyperbolic skyrmion II. The color of each arrow indicates the magnitude of S_z .

anisotropic. The two-component BECs should couple with each other to form the dipole structure. But how can we prove the presence of the two-extreme-value skyrmion in BECs? In the following content, we illuminate the method for creating the two-extreme-value skyrmions and explain the nontrivial phenomena.

III. STOCHASTIC PROJECTED GROSS-PITAEVSKII EQUATIONS FOR PSEUDO-SPIN-1/2 BECS WITH SPIN-ORBIT COUPLING

In real experiments, the zero temperature cannot be fully achieved. So the ultracold Bose gases are only partially condensed, with the noncondensed thermal cloud providing a source of dissipation and leading to damping excitations. Meanwhile, the evaporative cooling is a critical operation to obtain the condensate. Thus, it is necessary to refer to the finite-

temperature effect and a quenching process. The development of the stochastic projected Gross-Pitaevskii equation (SPGPE) gives us a way to describe the quenching process. The explicit formalism of the SPGPE has been presented in Refs. [29–32], and here we merely outline the particular method we use in this work. Generally, the SPGPE method divides the system into the coherent region and the incoherent region. This division is made by a projection operation \mathcal{P} , which restricts the dynamics of the BEC in the coherent region. The dynamics of the pseudo-spin-1/2 BECs can be described by the form

$$d\Psi_j = \mathcal{P} \left\{ -\frac{i}{\hbar} \hat{H}_j \Psi_j dt + \frac{\gamma_j}{k_B T} (\mu - \hat{H}_j) \Psi_j dt + dW_j \right\}, \quad (2)$$

where T is the final temperature, k_B is the Boltzmann constant, μ is the chemical potential, γ_j is the growth rate

TABLE I. The configuration of the skyrmion when we exchange the spin vectors and add minus to the vectors. The first column indicates the form of the spin vector of Eqs. (1). The column headings show the sign of the spin vector. The letter stands for the subfigure in Fig. 1, the radian in brackets denotes the counterclockwise rotation of the subfigure with the value, the ' symbol denotes the mapping with y axis, and the $-$ symbol denotes the exchange of the color (mapping with x - y plane).

| | (+, +, +) | (-, +, +) | (+, -, +) | (+, +, -) | (-, -, +) | (-, +, -) | (+, -, -) | (-, -, -) |
|-------------------|------------|---------------|--------------|-------------|--------------|--------------|-------------|--------------|
| (S_x, S_y, S_z) | $d(\pi/4)$ | b | a | $-d(\pi/4)$ | $d(-\pi/4)$ | $-b$ | $-a$ | $-d(-\pi/4)$ |
| (S_y, S_x, S_z) | c | $d(-\pi/2)$ | d | $-c$ | c' | $-d(-\pi/2)$ | $-d$ | $-c'$ |
| (S_x, S_z, S_y) | e | $f(\pi/2)$ | $-e(\pi)$ | $-e$ | $-f(-\pi/2)$ | $-f(\pi/2)$ | $e(\pi)$ | $f(-\pi/2)$ |
| (S_z, S_y, S_x) | $-f$ | $f(\pi)$ | $-e(-\pi/2)$ | f | $e(\pi/2)$ | $-f(\pi)$ | $e(-\pi/2)$ | $-e(\pi/2)$ |
| (S_z, S_x, S_y) | g | $-g(\pi)$ | $-g'(\pi)$ | $-g$ | g' | $g(\pi)$ | $g'(\pi)$ | $-g'$ |
| (S_y, S_z, S_x) | $g(\pi/2)$ | $-g'(-\pi/2)$ | $-g(-\pi/2)$ | $-g(\pi/2)$ | $g'(\pi/2)$ | $g'(-\pi/2)$ | $g(-\pi/2)$ | $-g'(\pi/2)$ |

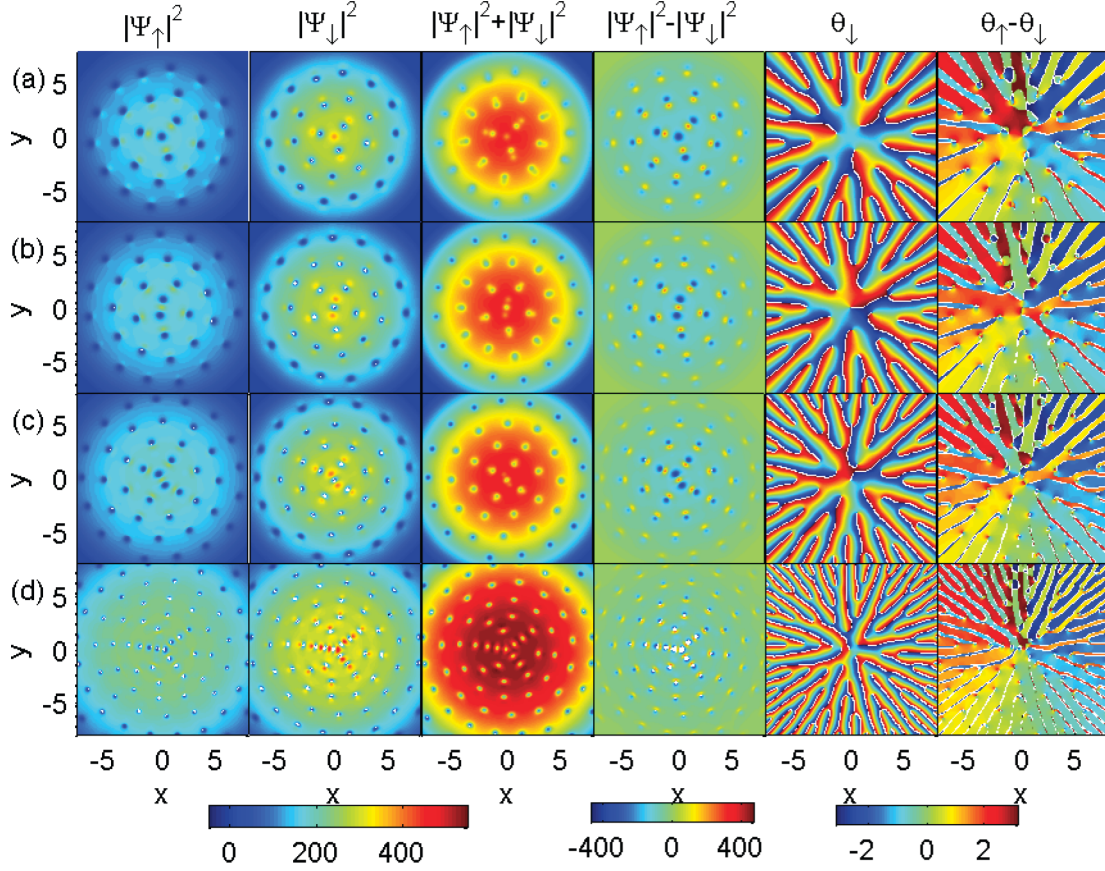


FIG. 2. (Color online) The densities and phases for the pseudo-spin-1/2 BEC of ^{87}Rb with SOC κ when the system reaches the equilibrium state. (a) $\kappa = 0.2$, (b) $\kappa = 0.5$, (c) $\kappa = 1.0$, and (d) $\kappa = 3.0$. Here, $\Omega = 0.5\omega$, $a_1 = 101.8a_B$, $a_2 = 0.8a_1$, and $a_{12} = 0.5a_1$. Note that the fifth column is the phase of the spin-down component, and the sixth column is the phase difference of the two components. The atom numbers (N_\uparrow , N_\downarrow) are approximately $(2.55 \times 10^4, 3.95 \times 10^4)$, $(2.82 \times 10^4, 4.09 \times 10^4)$, $(3.31 \times 10^4, 4.43 \times 10^4)$, and $(6.30 \times 10^4, 7.28 \times 10^4)$, respectively. The units of length and strength of the SOC are $\sqrt{\hbar/(m\omega)}$ and $\sqrt{\hbar\omega/m}$, respectively.

for the j th component, and dW_j is the complex Gaussian noise. Meanwhile, Ψ_j ($j = \uparrow, \downarrow$) denotes the macroscopic wave function of the atoms condensated in the spin-up and spin-down state, respectively, and

$$\begin{aligned} \hat{H}_\uparrow \Psi_\uparrow &= \left[-\frac{\hbar^2 \nabla^2}{2m} + V(r) + (g_1 |\Psi_\uparrow|^2 + g_{12} |\Psi_\downarrow|^2) \right] \Psi_\uparrow \\ &\quad - \Omega \hat{L}_z \Psi_\uparrow + (\kappa_x p_x - i\kappa_y p_y) \Psi_\downarrow, \\ \hat{H}_\downarrow \Psi_\downarrow &= \left[-\frac{\hbar^2 \nabla^2}{2m} + V(r) + (g_2 |\Psi_\downarrow|^2 + g_{12} |\Psi_\uparrow|^2) \right] \Psi_\downarrow \\ &\quad - \Omega \hat{L}_z \Psi_\downarrow + (\kappa_x p_x + i\kappa_y p_y) \Psi_\uparrow, \end{aligned} \quad (3)$$

with the coupling constants $g_1 = \frac{4\pi\hbar^2 a_1}{m}$, $g_2 = \frac{4\pi\hbar^2 a_2}{m}$, and $g_{12} = \frac{4\pi\hbar^2 a_{12}}{m}$. The trap potential is $V(r) = m\omega^2(x^2 + y^2)/2$. Ω is the rotation frequency, \hat{L}_z [$\hat{L}_z = -i\hbar(x\partial_y - y\partial_x)$] is the z component of the orbital angular momentum, and κ_x , κ_y denotes the strength of the SOC in the x , y direction, respectively. Meanwhile, p_x and p_y are the momentum operator in the x and y direction, respectively.

In Ref. [7], Lin *et al.* introduced a method to realize the SOC with BECs of ^{87}Rb . They select two internal “spin” states from within the ^{87}Rb $5S_{1/2}$, $F = 1$ ground electronic manifold,

and label them pseudo-spin-up and pseudo-spin-down. A pair of $\lambda_0 = 804.1$ nm Raman lasers, intersecting at $\theta = 90^\circ$ and detuned by δ from Raman resonance, couple these states with strength Ω_T . Ω_T and δ give rise to effective Zeeman fields along \hat{z} and \hat{y} , respectively. The SOC term results from the laser geometry, and the strength of the SOC is set by λ_0 and θ .

In numerical simulations, we choose the pseudo-spin-1/2 BECs of ^{87}Rb , where the mass of atom is $m = 144.42 \times 10^{-27}$ Kg. To obtain the initial states of each Ψ_j for evolution according to Eqs. (2), we sample the grand canonical ensemble for a free ideal Bose gas with the temperature T_0 and the chemical potential $\mu_{j,0}$. Meanwhile, the condensate band must lie below the energy cutoff $E_R > E_k = \frac{\hbar^2 |k|^2}{2m}$. Note that $k = 2\pi(n_x, n_y)/L$, where n_x , n_y are integers and L is the size of the computation domain. To simulate the quenching process, the final temperature and the chemical potential of the noncondensate band are altered to the values $T < T_0$ and $\mu > \mu_{j,0}$. Furthermore, we use the oscillator unit in the numerical computations. The length, time, and energy are scaled in units of $\sqrt{\frac{\hbar}{m\omega}}$, ω^{-1} , and $\hbar\omega$, respectively. In all of the simulations, the trapped frequency $\omega = 200 \times 2\pi$, the total number of the modes is n_x and $n_y = 280$, the energy cutoff is chosen at n_{xc} and $n_{yc} = 140$, the initial temperature

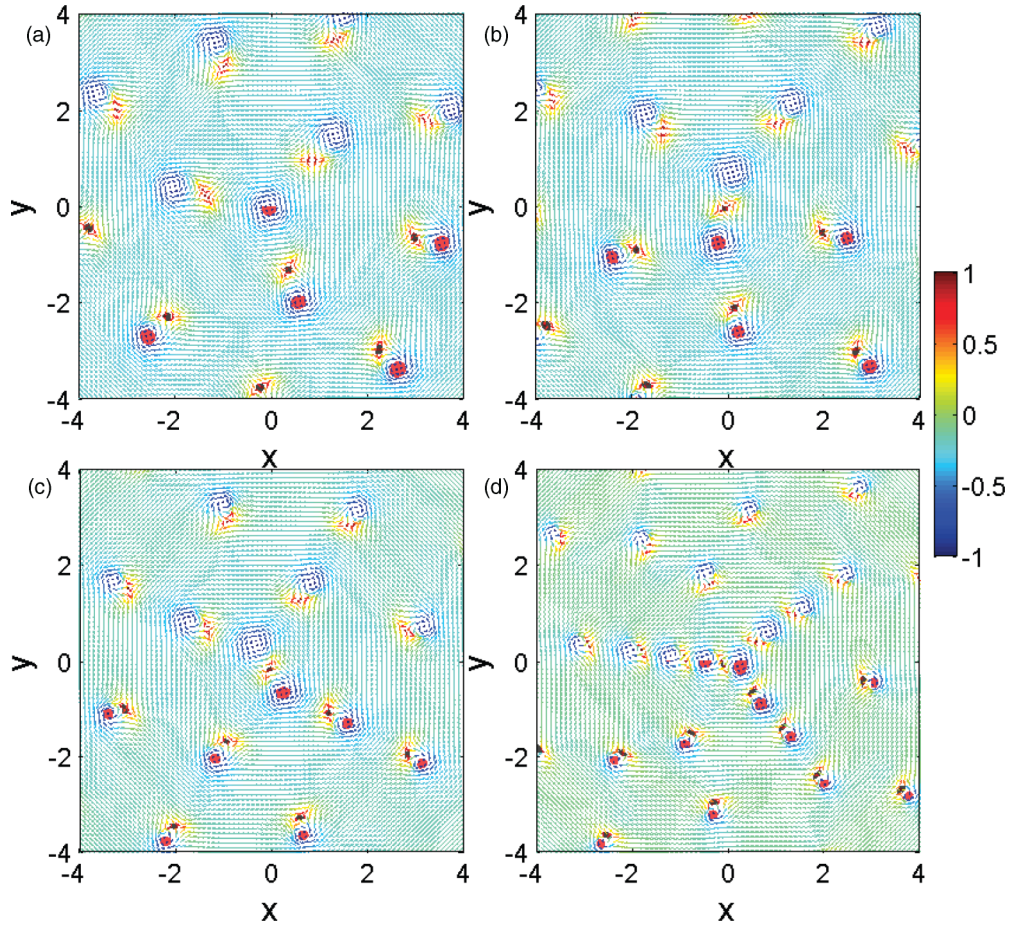


FIG. 3. (Color online) Spin texture of the pseudo-spin-1/2 BEC of ^{87}Rb with $\Omega = 0.5\omega$, $a_1 = 101.8a_B$, $a_2 = 0.8a_1$, and $a_{12} = 0.5a_1$. The color of each arrow indicates the magnitude of S_z . (a) $\kappa = 0.2$, (b) $\kappa = 0.5$, (c) $\kappa = 1$, and (d) $\kappa = 3.0$. The red and black spots are the center of the vortices formed by the spin-up and spin-down components, respectively. Note that we only mark the vortices in the $y > 0$ region in order to illuminate the spin texture and the position of the vortices clearly. The units of length and strength of the SOC are $\sqrt{\hbar/(m\omega)}$ and $\sqrt{\hbar\omega/m}$, respectively.

T_0 is 12 nK, the final temperature T is 5 nK, and we use $\frac{y_i}{k_B T} = 0.03$.

IV. RESULTS AND EXPLANATIONS

Generally speaking, almost all of the previous studies about BECs with SOC consider the equal contact interactions such as $g_1 = g_2 = g_{12}$, or only $g_1 = g_2$ as well as adjustment of the interspecies interaction g_{12} [8–15]. Theoretically, the interaction strengths g_1 , g_2 , and g_{12} are tunable by adjusting the s -wave scattering lengths a_1 , a_2 , and a_{12} through Feshbach resonances. To explore the potential nontrivial phenomena, we now perform our experiments with $a_1 \neq a_2 \neq a_{12}$. This consideration results in the population imbalance and induces some new physics. Since we consider the interactions $g_1 \neq g_2 \neq g_{12}$, the interspecies interaction plays an important role in determining the evolution of the two condensates. We must note that the two condensates consist of different components with the same mass m . Based on previous investigations, we can naturally divide the evolution into two cases: the miscible case where $g_{12} \leq \sqrt{g_1 g_2}$ and the immiscible case where $g_{12} > \sqrt{g_1 g_2}$.

A. Vortex-dipole and circular-hyperbolic skyrmion in rotating miscible BECs with spin-orbit coupling

We first consider the case $g_{12} \leq \sqrt{g_1 g_2}$, where $g_1 > g_2 > g_{12}$. We take BECs of ^{87}Rb as an example and assume $a_1 = 101.8a_B$, $a_2 = 0.8a_1$, and $a_{12} = 0.5a_1$. We set our model with $\mu_{j,0} = 5\hbar\omega$, $\mu = 35\hbar\omega$, $\kappa_x = \kappa_y = \kappa$ and the rotating frequency $\Omega = 0.5\omega$. Figure 2 displays the densities and phases obtained under the equilibrium state with various strengths of SOC. Just as previous experiments about the rotating BECs [29,30], there are some vortices in both components. The first and second columns are the density of the spin-up and spin-down components, respectively. The third column denotes the total density of the BECs, and the fourth column is the density difference of the two components. The fifth column indicates the phase of the spin-down component. Like the vortex lattice in a single-component BEC, there are some lines where the phases change discontinuously from red to blue, which corresponds to the branch cuts between the phases $-\pi$ and π . The ends represent phase defects. All of the lines extend to the outskirts of the BECs where the density of the BECs is almost negligible, and end with another defect which offers neither the energy nor the angular momentum to the system.

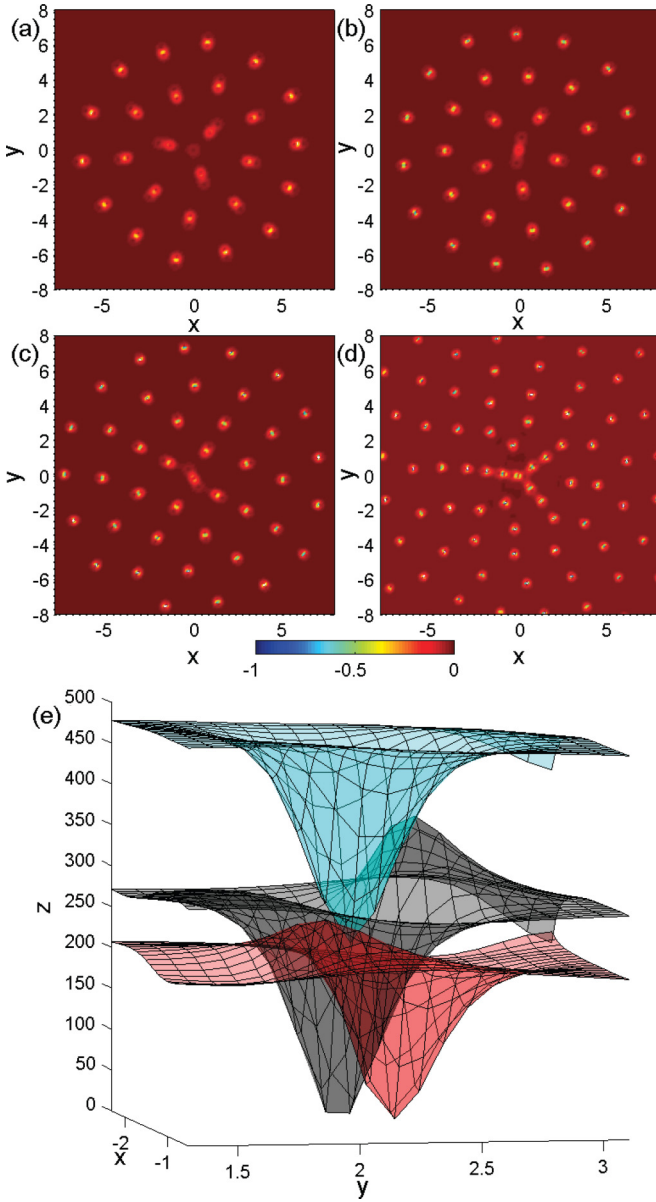


FIG. 4. (Color online) Topological charge density of pseudo-spin-1/2 BEC of ^{87}Rb with $\Omega = 0.5\omega$, $a_1 = 101.8a_B$, $a_2 = 0.8a_1$, and $a_{12} = 0.5a_1$. (a) $\kappa = 0.2$, (b) $\kappa = 0.5$, (c) $\kappa = 1.0$, and (d) $\kappa = 3.0$. (e) A scheme of the vortex dipole; the red and black surfaces denote the densities of the spin-up and spin-down components, respectively. The cyan surface is the total density of the BECs. The units of length and strength of the SOC are $\sqrt{\hbar/(m\omega)}$ and $\sqrt{\hbar\omega/m}$, respectively.

Generally speaking, the phases increase clockwise and then cut between the values $-\pi$ and π . The sixth column shows the phase difference between the two components. In [26,27], the “vortex molecule” has been discussed with the fixed phase difference of 2π . The unfixed phase difference in Fig. 2 indicates that the vortices do not form the so-called vortex molecule.

For a very weak SOC ($\kappa = 0.2$), the distribution of the vortices is relatively even. The relative proportional spacing of the vortices is destroyed as the SOC increases. When κ is

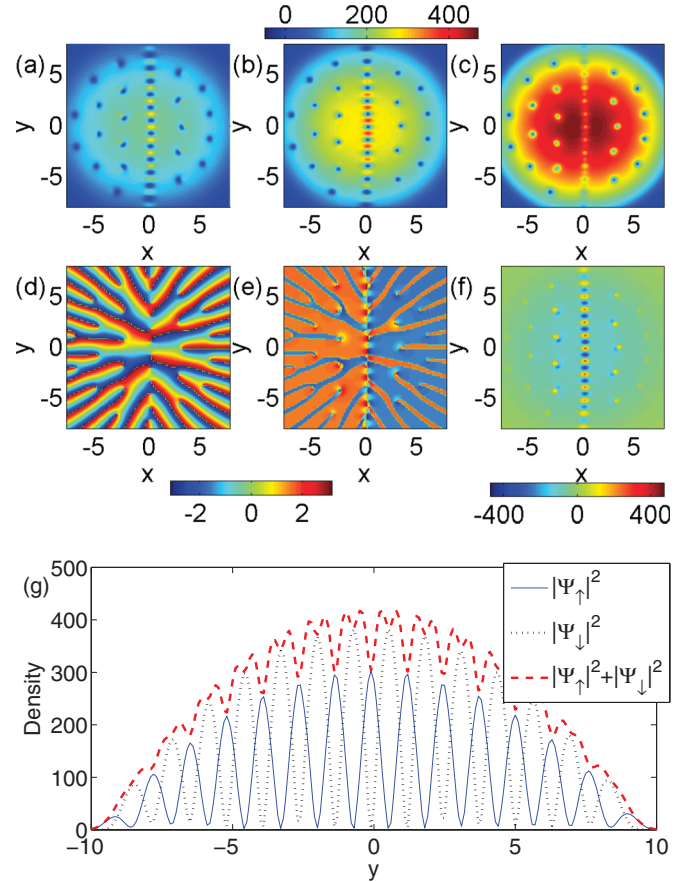


FIG. 5. (Color online) The densities and phases for the pseudo-spin-1/2 BECs of ^{87}Rb when the system reaches the equilibrium state, where $\Omega = 0.5\omega$, $\kappa_x = 0$, $\kappa_y = 1$, and $\mu = 35\hbar\omega$. (a) Density of the spin-up component, (b) density of the spin-down component, (c) total density of the BECs, (d) phase profile of the spin-up component, (e) phase difference of the two components, (f) density difference of the two components, and (g) density profile of the pseudo-spin-1/2 BECs in Figs. 5(a)–5(c), where $x = 0$. Here, $a_1 = 101.8a_B$, $a_2 = 0.8a_1$, and $a_{12} = 0.5a_1$. The atom numbers (N_\uparrow , N_\downarrow) are approximately $(2.98 \times 10^4, 4.26 \times 10^4)$. The units of length and strength of the SOC are $\sqrt{\hbar/(m\omega)}$ and $\sqrt{\hbar\omega/m}$, respectively.

greater than 1, some vortices tend to link one after another and form vortex lines locally from the center. Meanwhile, the particle number of the spin-up component is less than that of the spin-down component. As the SOC increases, the population imbalance tends to decrease. Thus, SOC restricts the population imbalance caused by the competition of contact interactions. In the third column, we can distinguish the local minima. The density difference of the spin-up and spin-down components shows that the two components form some dipoles locally. Especially for $\kappa = 3$, we can see some dipoles link one after another locally.

In our model, the particle number depends on the system itself. We do not fix the particle number and the ratio. Meanwhile, the rotation frequency is much less than ω . Thus, we do not obtain the giant vortex in the center of the system like those in Refs. [14,15].

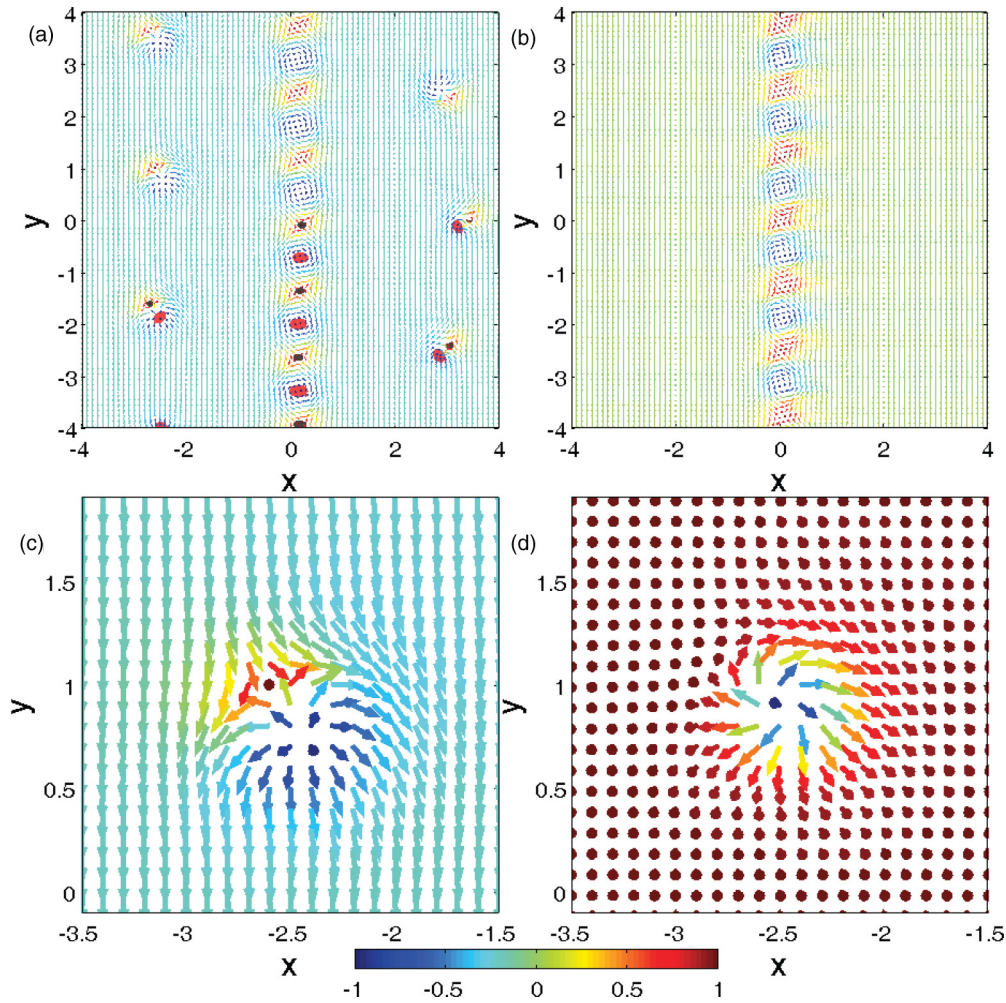


FIG. 6. (Color online) Spin texture of pseudo-spin-1/2 BECs of ^{87}Rb with $\Omega = 0.5\omega$, $\kappa_x = 0$, $\kappa_y = 1$, and $\mu = 35\hbar\omega$. (a) $a_1 = 101.8a_B$, $a_2 = 0.8a_1$, and $a_{12} = 0.5a_1$. The black and red spots are the centers of the vortices formed by the spin-up and spin-down components, respectively. Note that we only mark the vortices in the $y > 0$ region in order to illuminate the spin texture and the position of the vortices clearly. (b) Spin texture with Eqs. (6), where $c_1 = c_2 = 6$. (c) Enlarged plot of the radial-out and hyperbolic skyrmion in Fig. 5(a). (d) Radial-out and hyperbolic skyrmion transferred into the circular skyrmion under the transformation of the $(S_x, S_z, -S_y)$. The units of length and strength of the SOC are $\sqrt{\hbar/(m\omega)}$ and $\sqrt{\hbar\omega/m}$, respectively.

We now discuss the spin texture in the above experiments. The spin texture [26,27,33,34] is defined by

$$\begin{aligned}
 \mathbf{S}_x &= (\Psi_\uparrow^* \Psi_\downarrow + \Psi_\downarrow^* \Psi_\uparrow) / |\Psi|^2, \\
 \mathbf{S}_y &= -i(\Psi_\uparrow^* \Psi_\downarrow - \Psi_\downarrow^* \Psi_\uparrow) / |\Psi|^2, \\
 \mathbf{S}_z &= (|\Psi_\uparrow|^2 - |\Psi_\downarrow|^2) / |\Psi|^2.
 \end{aligned} \quad (4)$$

Figure 3 shows the spin texture of the miscible case with various strengths of SOC. Some circular-hyperbolic skyrmions encircle the center in Figs. 3(a)–3(d). We mark the positions of the vortices with color spots only in the region $y < 0$. Obviously, the circular structures are related to the vortices of the spin-up component and the hyperbolic structures are related to the vortices of the spin-down component. Thus, they can be viewed as the vortex-dipole structure. Figure 4(e) shows a scheme of the vortex-dipole structure with the densities. The red, black, and cyan colors denote the spin-up component, spin-down component, and their sum, respectively. If we draw a line through the circular part and the hyperbolic part of

the skyrmion, the line passes through the center. Meanwhile, the center is a circular structure in Figs. 3(a) and 3(c), but a hyperbolic structure in Fig. 3(d). These properties mean the difference of one between the number of vortices in the two components. Furthermore, the arrows form a big circular pattern in the whole BECs.

The corresponding topological charge densities are displayed in Figs. 4(a)–4(d), respectively. We first point out the difference between the circular-hyperbolic skyrmion and the meron pair. For the meron pair, the topological charge density is distributed anisotropically so that the distribution is elongated along the direction of polarization of the meron pair [26,27,33,34]. When the SOC is very weak ($\kappa = 0.2$), the topological charge density tends to be elongated along the radius. This indicates that the “circular-hyperbolic skyrmions” process the properties of the circular-hyperbolic meron pair. When SOC increases, the elongated effect of the topological charge density disappears. Thus, we can view the spin texture in Figs. 4(a) and 4(b) as the mixtures between circular-

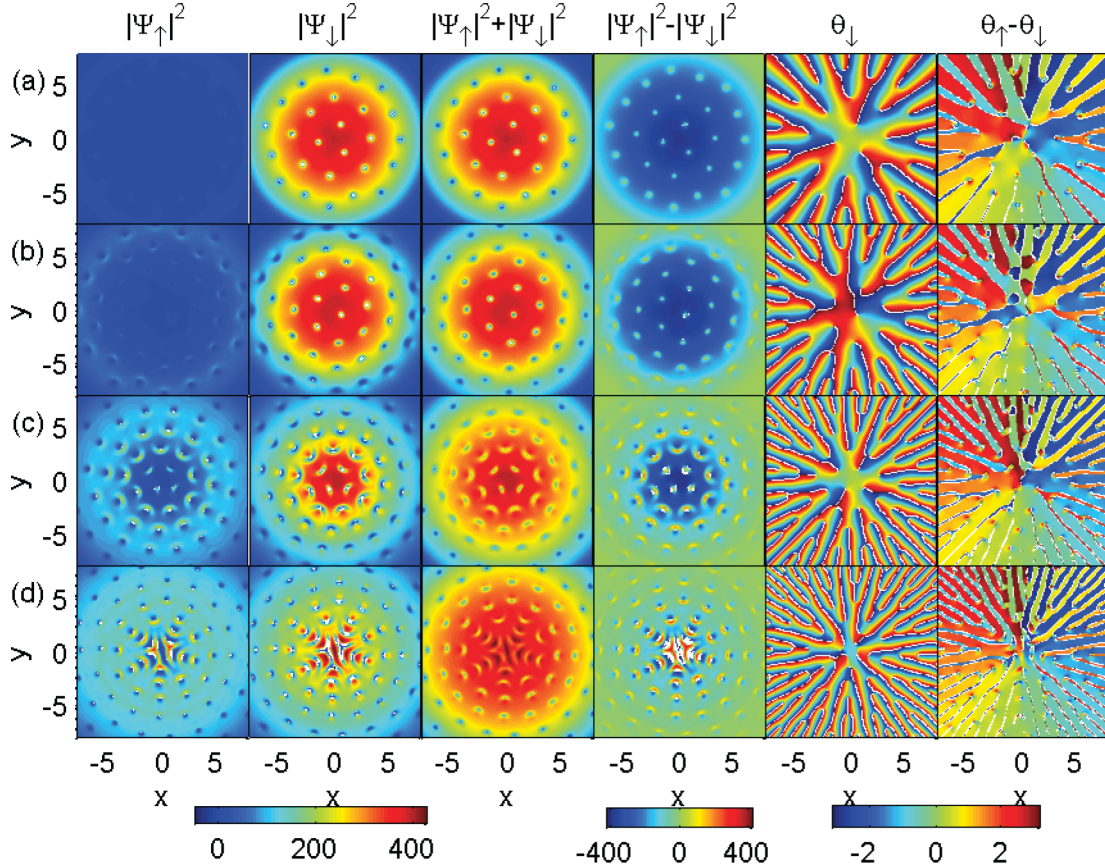


FIG. 7. (Color online) The densities and phases for the pseudo-spin-1/2 BECs of ^{87}Rb with SOC κ when the system reaches the equilibrium state. (a) $\kappa = 0.2$, (b) $\kappa = 1.0$, (c) $\kappa = 2.0$, and (d) $\kappa = 3.0$. Here, $\Omega = 0.5\omega$, $a_1 = 101.8a_B$, $a_2 = 0.8a_1$, and $a_{12} = 1.2a_1$. Note that the fifth column is the phase of the spin-down component, and the sixth column is the phase difference of the two components. The atom numbers (N_\uparrow , N_\downarrow) are approximately $(500, 5.34 \times 10^4)$, $(0.95 \times 10^4, 4.81 \times 10^4)$, $(2.54 \times 10^4, 4.39 \times 10^4)$, and $(4.11 \times 10^4, 5.05 \times 10^4)$, respectively. The units of length and strength of the SOC are $\sqrt{\hbar/(m\omega)}$ and $\sqrt{\hbar\omega/m}$, respectively.

hyperbolic skyrmions and circular-hyperbolic meron pairs. The spin texture should be the circular-hyperbolic meron pairs when $\kappa = 0$. References [26,27] obtained the meron pairs without SOC and pointed out that the texture can form the “circular-hyperbolic” pair, while the spin textures are circular-hyperbolic skyrmions when $\kappa \geq 1$. The circular-hyperbolic skyrmions tend to link one after another and form the circular-hyperbolic skyrmion arrays, especially when the SOC is strong enough ($\kappa = 3$).

We indeed find the circular-hyperbolic skyrmion, which is related to the vortex dipole. In Fig. 2 (third column), we can detect some local minima of the total densities. Furthermore, we also find that the phase difference between the two components is not the fixed value of 2π . Thus, the coupling of the vortex of the two components does not come from the phase, but from the SOC. Certainly, the vortex dipole is not the coreless Anderson vortex (vortex molecule) [26,27], which does not have the singularity. Therefore, the rotation factually only causes the creation of the vortices. SOC induces the coupling of the vortex formed by different components.

In the above experiments, the SOC is isotropic, where $\kappa_x = \kappa_y$. We can deduce that if we turn off the SOC in one direction but maintain it in the other direction, then the big circular structure would be broken. The circular-hyperbolic

skyrmion should link to form a chain. Now, we perform the experiment with BECs of ^{87}Rb , where $\kappa_x = 0$, $\kappa_y = 1$, $\Omega = 0.5\omega$, $a_1 = 101.8a_B$, $a_2 = 0.8a_1$, $a_{12} = 0.5a_1$, $\mu_{j,0} = 5\hbar\omega$, and $\mu = 35\hbar\omega$. Figure 5 shows the densities and phases under the equilibrium state. We can see that the vortices form a chain in the center along the y axis. Furthermore, some vortices distribute relatively equal in other region of the BECs. Figure 5(g) is the density profile along the y axis, where $x = 0$. It shows that the vortices of the two components interlace with each other. Meanwhile, the total density is concavo-convex.

Figure 6 shows the spin texture of BECs with SOC only along the y axis. In Fig. 6(a), the circular-hyperbolic skyrmions link one after another and form a chain. The main direction of the arrows is down in the region $x < 0$, and is up in the region $x > 0$. We can use the following equations to approximately present the center chain of the circular-hyperbolic skyrmion:

$$\begin{aligned} S_{0x} &= \frac{2 \sin(5y) \sqrt{1 + e^{c_1 x} \sin^2(c_2 y)}}{e^{c_1 x} + e^{-c_1 x} + \sin^2(c_2 y)}, \\ S_{0y} &= \frac{e^{c_1 x} - e^{-c_1 x} - \sin^2(c_2 y)}{e^{c_1 x} + e^{-c_1 x} + \sin^2(c_2 y)}, \\ S_{0z} &= \frac{2 \cos(5y) \sqrt{1 + e^{c_1 x} \sin^2(c_2 y)}}{e^{c_1 x} + e^{-c_1 x} + \sin^2(c_2 y)}. \end{aligned} \quad (5)$$

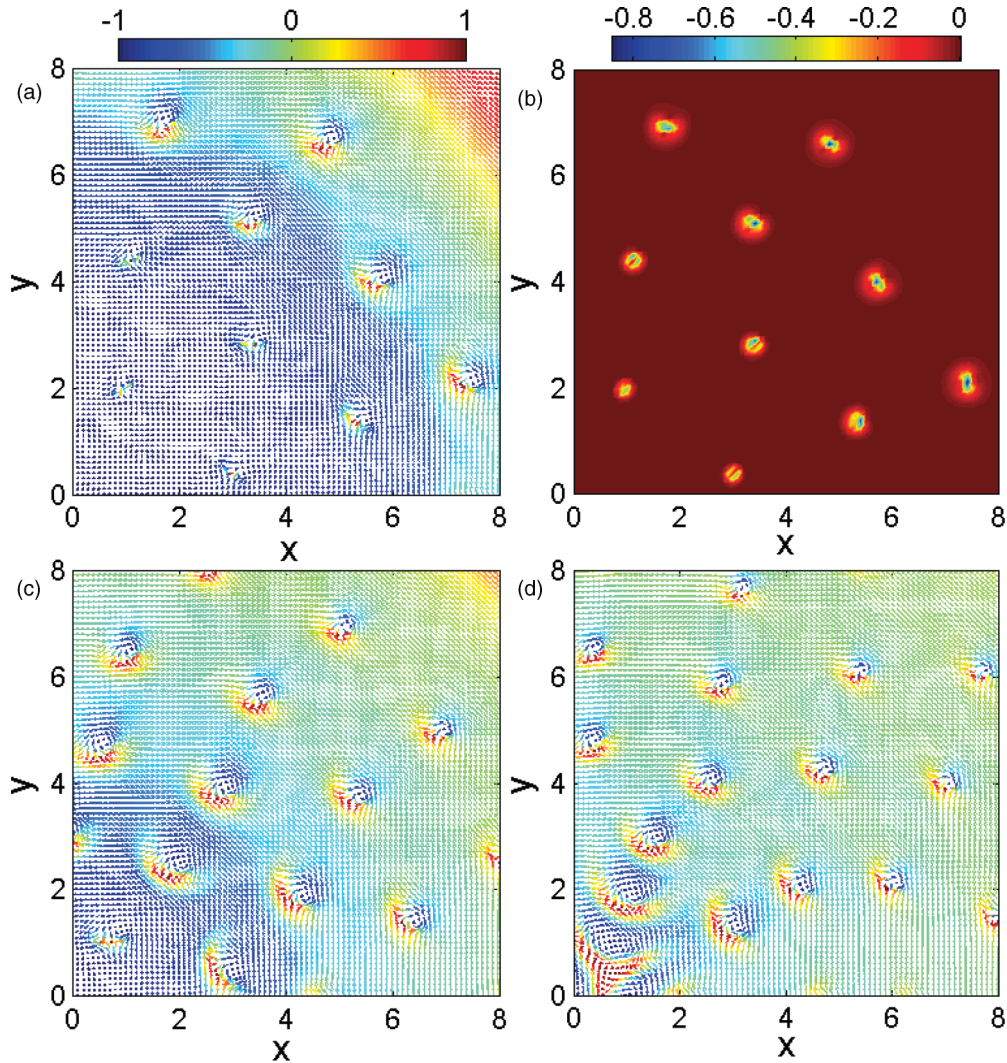


FIG. 8. (Color online) Spin texture of pseudo-spin-1/2 BECs of ^{87}Rb with $\Omega = 0.5\omega$, $a_1 = 101.8a_B$, $a_2 = 0.8a_1$, and $a_{12} = 1.2a_1$. (a) $\kappa = 1.0$, (b) the corresponding topological charge density of Fig. 8(a), (c) $\kappa = 2.0$, and (d) $\kappa = 3.0$. The units of length and strength of the SOC are $\sqrt{\hbar/(m\omega)}$ and $\sqrt{\hbar\omega/m}$, respectively.

Figure 6(b) is the spin texture with Eqs. (5). Comparing it with Fig. 6(a), the formation of the two spin textures is very similar. This indicates that Eqs. (5) can approximately describe the skyrmion chain in our simulation. Figure 6(c) is an enlarged plot of the hyperbolic-radial(out) skyrmion at $(-2.5, 1)$. With the transformation $(\mathbf{S}_{0x}, \mathbf{S}_{0z}, -\mathbf{S}_{0y})$, we obtain Fig. 6(d), which is a typical circular skyrmion. In [27], the asymmetric vortex molecule is studied and is found to have a phase difference of 2π . The vortex molecule is induced by the phase coupling. Here, we find that the vortex dipoles do not have the phase coupling of 2π . The vortex dipole derives from the SOC. Accordingly, we do not view the texture to be the “radial-hyperbolic” pair of merons, but the radial-hyperbolic skyrmion.

We obtain Eqs. (5) to characterize the skyrmion chain intuitively according to the properties of Fig. 6(a). In the region of $x < 0$, the main direction of the arrows is pointing down, while in the region of $x > 0$, the arrows point up. These properties indicate that the spin vector \mathbf{S}_{0y} can be approximately described by a function $(\tanh x)$. Meanwhile,

the circular-hyperbolic skyrmion chain along the y axis shows a periodic change only in the y axis. The simplest periodical function along the y axis is $\sin cy$. Thus, we couple the two functions and obtain \mathbf{S}_{0y} . According to the condition $|\mathbf{S}_{0x}|^2 + |\mathbf{S}_{0z}|^2 = 1 - |\mathbf{S}_{0y}|^2$, we can obtain an expression, $\frac{2\sqrt{1+e^{c_1x}\sin^2(c_2y)}}{e^{c_1x}+e^{-c_1x}+\sin^2(c_2y)}$. \mathbf{S}_{0x} and \mathbf{S}_{0y} should be related to the expression. Similarly, the simplest couple is the sine and cosine function. Therefore, we obtain Eqs. (5).

B. Vortex-dipole and circular-hyperbolic skyrmion in rotating immiscible BECs with spin-orbit coupling

We now study the immiscible BECs with SOC under the rotating and rapidly quenched experiment. We assume the atom is ^{87}Rb , where $a_1 = 101.8a_B$, $a_2 = 0.8a_1$, and $a_{12} = 1.2a_1$. The initial and final chemical potentials are $\mu_{j,0} = 5\hbar\omega$ and $\mu = 35\hbar\omega$, respectively. The rotating frequency is $\Omega = 0.5\omega$. Figure 7 shows the densities and phases of the immiscible case with isotropic SOC, where $\kappa_x = \kappa_y = \kappa$. The two components

are the phase separation without SOC. Compared with Fig. 2, the population imbalance is considerably larger when the SOC is weak ($\kappa = 0.2$). This is understood because the more the spin-up component is, the higher the energy of the system is, due to the interaction energy. The immiscible property causes the outer spin-up component to be easily kicked out as the noncondensate. Thus, the mixtures play like a single condensate and the vortex lattice is hexagonal. When the strength of the SOC is increased, the spin-up component increases. But it mainly occurs at the outskirts of the system, while the spin-down component locates at the center. SOC plays a role in pulling the spin-up component into the center of the system. When the SOC is up to 3, the two components look like they are completely mixed. Then, the two components are of the same order of magnitude. Therefore, the competition between the interspecies and intraspecies interaction causes the population imbalance, while the SOC restricts the disproportion.

If we examine the density difference of the two components (the fourth column), we find that the pattern changes from the spots lattice into the dipole lattice when the SOC varies from 0.2 to 3. Meanwhile, the emergence of the dipole starts from the outskirts of the system. Because the spin-up component tends to locate at the outskirts of the system, the dipole easily occurs at the outskirt region of the system [see Figs. 7(c) and 7(d)]. By increasing the SOC, more spin-up component is pulled into the system and the dipoles extend into the center. Furthermore, there is a trend that the disfigurement in the BEC changes from the hole into the stripe as the SOC increases (see the total density). Our experiments also imply that the population imbalance exists in real experiments.

Figure 8 shows the spin texture of the immiscible case with various strengths of SOC. In Fig. 8(a), most of the arrows stands up. In fact, the big arrow circle occurs in the outskirts of the system. The hyperbolic skyrmion occurs in the center, while the circular-hyperbolic skyrmion is formed at the outskirts. Figure 8(b) is the corresponding topological charge density of Fig. 8(a). Here, the topological charge density has not been elongated at all. Thus, the spin texture is the typical circular-hyperbolic skyrmion, hyperbolic skyrmion, etc. As the SOC increases, more spin-up component is pulled into the center, and more hyperbolic skyrmion transfers into the circular-hyperbolic skyrmion. Thus, we can see a transformation between the circular-hyperbolic skyrmion and the hyperbolic skyrmion as the radius decreases.

We do not show the spin textures when $\kappa < 1$ because the particle number of the spin-up component is much less than that of the spin-down one. The pseudo-spin-1/2 BECs behave like the single-component one. Although some spin-up atoms locate at the center of the vortex formed by the spin-down component, the particle number is so little that we prefer to view the whole BECs as the single-component one.

The above experiments focus on the isotropy system. We can turn off the strength of the SOC in the x direction and maintain it in the y direction. In Fig. 4, we only set the SOC in the y axis and turn off the SOC in the x direction with the miscible BECs. We can see that the vortices form an array in the center along the y axis. Figure 9 shows the results of the immiscible case. In Fig. 9(a), some spots distribute with the hexagonal lattice. In fact, there are some vortices formed

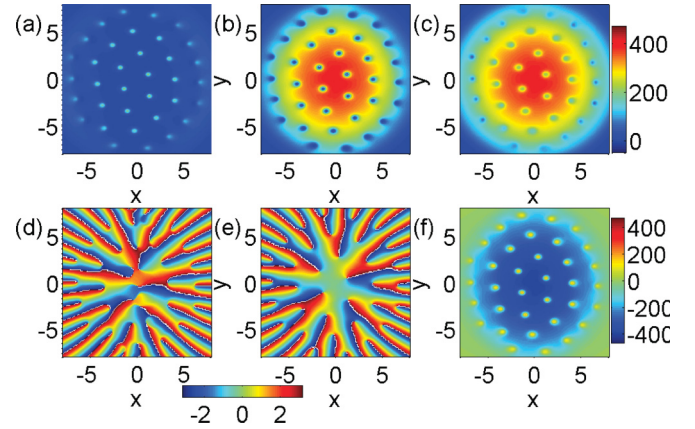


FIG. 9. (Color online) The densities and phases for the pseudo-spin-1/2 BECs of ^{87}Rb when the system reaches the equilibrium state, where $\Omega = 0.5\omega$, $\kappa_x = 0$, $\kappa_y = 1$, and $\mu = 35\hbar\omega$. (a) Density of the spin-up component, (b) density of the spin-down component, (c) total density of the BECs, (d) phase profile of the spin-up component, (e) phase profile of the spin-down component, and (f) density difference of the two components. Here, $a_1 = 101.8a_B$, $a_2 = 0.8a_1$, and $a_{12} = 1.2a_1$. The atom numbers (N_\uparrow , N_\downarrow) are approximately $(6.5 \times 10^3, 4.94 \times 10^4)$. The units of length and strength of the SOC are $\sqrt{\hbar/(m\omega)}$ and $\sqrt{\hbar\omega/m}$, respectively.

by the spin-up condensate. But the density is so low that it is hard to distinguish them from the density. Here, the vortices do not form the array along the y axis, but distribute relatively equal. The spots formed by the spin-up condensate locate at the vortices formed by the spin-down condensate. According to Fig. 9(f), no dipole structure occurs in this system. Certainly, the spin-up component is so little that the vortices in the mixture play like those in the single-component BEC. Thus, the vortices lattice is hexagonal in Fig. 9(b).

The difference between Fig. 4 and Fig. 9 comes from the interspecies interactions. Because the two components are immiscible, the spin-up component cannot collect near the

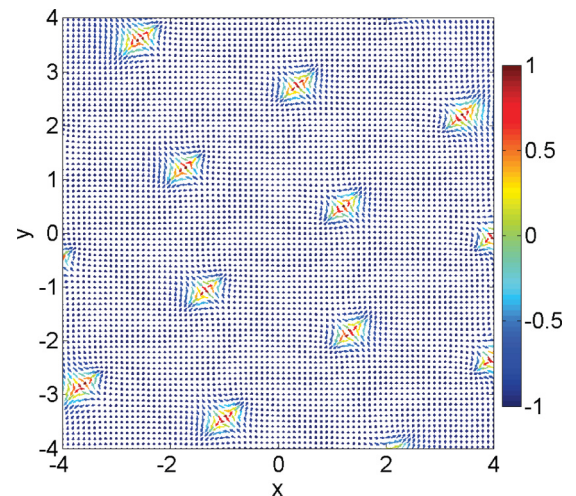


FIG. 10. (Color online) Spin texture of pseudo-spin-1/2 BECs of ^{87}Rb with $\Omega = 0.5\omega$, $\kappa_x = 0$, $\kappa_y = 1$, $\mu = 35\hbar\omega$, $a_1 = 101.8a_B$, $a_2 = 0.8a_1$, and $a_{12} = 1.2a_1$. The units of length and strength of the SOC are $\sqrt{\hbar/(m\omega)}$ and $\sqrt{\hbar\omega/m}$, respectively.

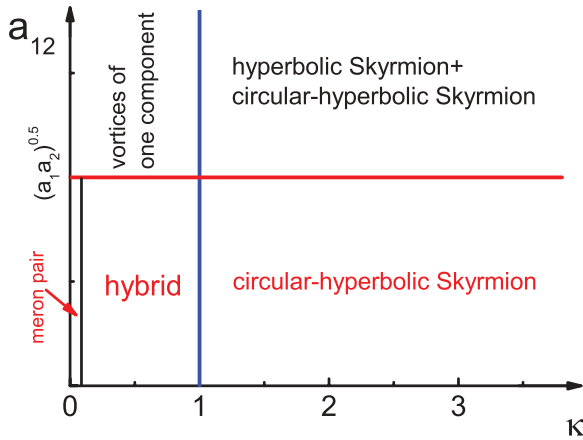


FIG. 11. (Color online) The scheme of phase diagrams of the products in pseudo-spin-1/2 BECs with a_{12} ($a_1 \neq a_2$) and the SOC strength κ ($\kappa_x = \kappa_y = \kappa$). The rotation frequency is $\Omega = 0.5\omega$. The unit of strength of the SOC is $\sqrt{\hbar\omega/m}$.

center. It mainly distributes in the vortices that are formed by the spin-down component. So, only the hyperbolic skyrmion lattice occurs in Fig. 10. The arrow around the hyperbolic skyrmion is standing up in Fig. 10. This is the principal difference between the hyperbolic skyrmion and the circular-hyperbolic one, where the arrows around the skyrmion are horizontal or vertical.

Figure 11 is the scheme of the phase diagram of the pseudo-spin-1/2 BECs with various products in our experiments. SOC plays an important role in inducing the circular-hyperbolic skyrmion. When $a_{12} \leq \sqrt{a_1 a_2}$, SOC (≥ 1) causes the vortex of different components to couple with each other and form the circular-hyperbolic skyrmions. If the SOC is too weak (~ 0), then the topological charge density is easy to elongate along the vortex pair. The spin texture is a meron pair. Between the two cases, we observe the hybrid of a circular-hyperbolic skyrmion and a circular-hyperbolic meron pair. When $a_{12} > \sqrt{a_1 a_2}$ and SOC is weak (< 1), the BECs are easily imbalanced because of the phase separation and the competition between the different intraspecies interactions. So the BECs behave like the single-component one with the vortices. For stronger SOC (> 1), we obtain the circular-hyperbolic skyrmion in the

outskirts of the BECs and the hyperbolic skyrmions remain in the center. Certainly, the circular-hyperbolic skyrmion would not appear if the rotation is too weak to excite the vortices.

Our study mainly focuses on the creation of the nontrivial type of skyrmion. We start with the analysis of the possibility of the circular-hyperbolic skyrmion according to the normal skyrmion solution. Our analysis indicates that the normal skyrmion solution can change into four single-center skyrmion configurations and three two-center skyrmion configurations. Generally speaking, by exploring the rotating BECs with SOC, we find the two types of skyrmions: the circular-hyperbolic skyrmion and the hyperbolic-radial skyrmion.

V. CONCLUSION

We have studied systematically the circular-hyperbolic skyrmion in the rotating pseudo-spin-1/2 BECs with SOC. Some interesting phenomena are found. We find that the circular-hyperbolic skyrmion lattice can occur in the miscible BECs with SOC. Unlike the normal skyrmion, which has only one center, the circular-hyperbolic skyrmion has two centers and is related to the vortex dipole. The stronger the SOC is, the more likely the circular-hyperbolic skyrmions tend to link one after another and form chains. We also design an experimental scheme with SOC only in the y direction to obtain a single circular-hyperbolic skyrmion chain, while in the immiscible BECs, the phase-separation effect causes the circular-hyperbolic skyrmions mainly to occur in the outskirts of the BECs. In the center of the BECs, the hyperbolic skyrmion occurs. By increasing the strength of the SOC, more spin-up component is pulled into the center and the appearance of the circular-hyperbolic skyrmion becomes easier. Our study provides the experimental conditions to observe these phenomena in future experiments.

ACKNOWLEDGMENTS

This work was supported by the NKBRSCF under Grants No. 2011CB921502, No. 2012CB821305, No. 2009CB930701, and No. 2010CB922904; the NSFC under Grants No. 10934010 and No. 60978019; and the NSFC-RGC under Grants No. 11061160490 and No. 1386-N-HKU748/10.

-
- [1] Y. K. Kato, R. C. Myers, A. C. Gossard, and D. D. Awschalom, *Science* **306**, 1910 (2004).
 - [2] M. König, S. Wiedmann, C. Brüne, A. Roth, H. Buhmann, L. W. Molenkamp, X.-L. Qi, and S.-C. Zhang, *Science* **318**, 766 (2007).
 - [3] C. L. Kane and E. J. Mele, *Phys. Rev. Lett.* **95**, 146802 (2005).
 - [4] B. A. Bernevig, T. L. Hughes, and S.-C. Zhang, *Science* **314**, 1757 (2006).
 - [5] D. Hsieh, D. Qian, L. Wray, Y. Xia, Y. S. Hor, R. J. Cava, and M. Z. Hasan, *Nature (London)* **452**, 970 (2008).
 - [6] Y.-J. Lin, R. L. Compton, K. Jiménez-García, J. V. Porto, and I. B. Spielman, *Nature (London)* **462**, 628 (2009).
 - [7] Y.-J. Lin, K. Jiménez-García, and I. B. Spielman, *Nature (London)* **471**, 83 (2011).
 - [8] C. Wang, C. Gao, C.-M. Jian, and H. Zhai, *Phys. Rev. Lett.* **105**, 160403 (2010).
 - [9] T.-L. Ho and S. Z. Zhang, *Phys. Rev. Lett.* **107**, 150403 (2011).
 - [10] C.-M. Jian and H. Zhai, *Phys. Rev. B* **84**, 060508(R) (2011).
 - [11] S. Sinha, R. Nath, and L. Santos, *Phys. Rev. Lett.* **107**, 270401 (2011).
 - [12] H. Hu, B. Ramachandhran, H. Pu, and X.-J. Liu, *Phys. Rev. Lett.* **108**, 010402 (2012).
 - [13] C. Wu, I. Mondragon-Shem, and X. F. Zhou, *Chin. Phys. Lett.* **28**, 097102 (2011).
 - [14] X.-Q. Xu and J. H. Han, *Phys. Rev. Lett.* **107**, 200401 (2011).
 - [15] X.-F. Zhou, J. Zhou, and C. Wu, *Phys. Rev. A* **84**, 063624 (2011).
 - [16] T. H. R. Skyrme, *Proc. R. Soc. A* **260**, 127 (1961).
 - [17] T. H. R. Skyrme, *Nucl. Phys.* **31**, 556 (1962).

- [18] P. W. Anderson and G. Toulouse, *Phys. Rev. Lett.* **38**, 508 (1977).
- [19] A. Schmeller, J. P. Eisenstein, L. N. Pfeiffer, and K. W. West, *Phys. Rev. Lett.* **75**, 4290 (1995).
- [20] D. C. Wright and N. D. Mermin, *Rev. Mod. Phys.* **61**, 385 (1989).
- [21] A. Neubauer, C. Pfleiderer, B. Binz, A. Rosch, R. Ritz, P. G. Niklowitz, and P. Böni, *Phys. Rev. Lett.* **102**, 186602 (2009).
- [22] X. Z. Yu, Y. Onose, N. Kanazawa, J. H. Park, J. H. Han, Y. Matsui, N. Nagaosa, and Y. Tokura, *Nature (London)* **465**, 901 (2010).
- [23] N. D. Mermin and T.-L. Ho, *Phys. Rev. Lett.* **36**, 594 (1976).
- [24] U. Al Khawaja and H. Stoof, *Nature (London)* **411**, 918 (2001).
- [25] U. A. Khawaja and H. T. C. Stoof, *Phys. Rev. A* **64**, 043612 (2001).
- [26] K. Kasamatsu, M. Tsubota, and M. Ueda, *Phys. Rev. Lett.* **93**, 250406 (2004).
- [27] K. Kasamatsu, M. Tsubota, and M. Ueda, *Phys. Rev. A* **71**, 043611 (2005).
- [28] C.-F. Liu and W.-M. Liu, *Phys. Rev. A* **86**, 033602 (2012).
- [29] A. S. Bradley, C. W. Gardiner, and M. J. Davis, *Phys. Rev. A* **77**, 033616 (2008).
- [30] S.-W. Su, C.-H. Hsueh, I.-K. Liu, T.-L. Horng, Y.-C. Tsai, S.-C. Gou, and W. M. Liu, *Phys. Rev. A* **84**, 023601 (2011).
- [31] S. J. Rooney, A. S. Bradley, and P. B. Blakie, *Phys. Rev. A* **81**, 023630 (2010).
- [32] S.-W. Su, I.-K. Liu, Y.-C. Tsai, W. M. Liu, and S.-C. Gou, *Phys. Rev. A* **86**, 023601 (2012).
- [33] T. Mizushima, K. Machida, and T. Kita, *Phys. Rev. Lett.* **89**, 030401 (2002).
- [34] T. Mizushima, N. Kobayashi, and K. Machida, *Phys. Rev. A* **70**, 043613 (2004).